remote sensing

MDPI

Article

Methodology for Lidar Monitoring of Biomass Burning Smoke in Connection with the Land Cover

Mariana Adam [1,*], Konstantinos Fragkos [1,2], Stavros Solomos [3], Livio Belegante [1], Simona Andrei [1], Camelia Talianu [1], Luminița Mărmureanu [1], Bogdan Antonescu [1], Dragos Ene [2], Victor Nicolae [1] and Vassilis Amiridis [4]

[1] National Institute of Research and Development for Optoelectronics INOE 2000, 077125 Magurele, Romania
[2] ERATOSTHENES Centre of Excellence, 3036 Limassol, Cyprus
[3] Research Centre for Atmospheric Physics and Climatology, Academy of Athens, 10679 Athens, Greece
[4] National Observatory of Athens, 15236 Penteli, Greece
* Correspondence: mariana.adam@inoe.ro

Abstract: Lidar measurements of 11 smoke layers recorded at Măgurele, Romania, in 2014, 2016, and 2017 are analyzed in conjunction with the vegetation type of the burned biomass area. For the identified aerosol pollution layers, the mean optical properties and the intensive parameters in the layers are computed. The origination of the smoke is estimated by the means of the HYSPLIT dispersion model, taking into account the location of the fires and the injection height for each fire. Consequently, for each fire location, the associated land cover type is acquired by satellite-derived land cover products. We explore the relationship between the measured intensive parameters of the smoke layers and the respective land cover of the burned area. The vegetation type for the cases we analyzed was either broadleaf crops or grasses/cereals. Overall, the intensive parameters are similar for the two types, which can be associated with the fact that both types belong to the broader group of agricultural crops. For the cases analyzed, the smoke travel time corresponding to the effective predominant vegetation type is up to 2.4 days.

Keywords: lidar; biomass burning; land cover; HYSPLIT; MODIS; ERA5; FLEXPART

check for updates

Citation: Adam, M.; Fragkos, K.; Solomos, S.; Belegante, L.; Andrei, S.; Talianu, C.; Mărmureanu, L.; Antonescu, B.; Ene, D.; Nicolae, V.; et al. Methodology for Lidar Monitoring of Biomass Burning Smoke in Connection with the Land Cover. *Remote Sens.* **2022**, *14*, 4734. https://doi.org/10.3390/rs14194734

Academic Editors: Simone Lolli, Daniel Pérez-Ramírez and Haiyun Xia

Received: 29 July 2022
Accepted: 19 September 2022
Published: 22 September 2022

Publisher's Note: MDPI stays neutral with regard to jurisdictional claims in published maps and institutional affiliations.

Copyright: © 2022 by the authors. Licensee MDPI, Basel, Switzerland. This article is an open access article distributed under the terms and conditions of the Creative Commons Attribution (CC BY) license (https://creativecommons.org/licenses/by/4.0/).

1. Background

Biomass burning (BB) constitutes one of the major sources of aerosols and often represents a major pollution event in the planetary boundary layer (PBL), free troposphere (FT), or even in the stratosphere. Smoke particles can have either a direct or indirect radiative effect [1]. At ground level, the visibility can diminish [2] while the air quality degrades [3] and health-related issues for humans arise [4]. Nicolae et al. [5] analyzed data collected by 17 stations with collocated lidars and sun photometers over Europe during an 11-year period (2008–2018) and showed that smoke was the predominant aerosol type (37%) over Europe, followed by continental aerosols (25%).

Within this context, we performed an extensive literature search related to the vegetation type of the burned area and its impact on various remote measurements, especially on lidar records. In order to quantify a potential link between the type of burned vegetation and the remote measured smoke, extensive measurements related to the microphysical and chemical properties of the emitted smoke, smoke's injection height, as well as the meteorological conditions of the transported air mass should, ideally, be known. There are several studies which involved to some extent the information about land cover.

Shi et al. [6] studied the BB aerosol characteristics for three vegetation types (forest and peat, grass and shrub, and mixed) in different aging periods (<24 h and >24 h) using 18 years of Aeronet data, MODIS fire products, and the HYSPLIT model. The radiative forcing at the TOA (top of the atmosphere) was found negative for all the vegetation types, while an enhancement in the negative radiative forcing efficiency was found for aging

aerosol. For the three land cover types considered, the following were found: the BC (black carbon) content dropped during aging while SSA (single scattering albedo), fine-mode median radius, and asymmetry factor increased during aging (>24 h). Forest and peat had the lowest volume fraction of BC (1.08%) and the highest fine-mode median radius (0.182 μm), while the grass and shrub had the highest fraction of BC (3.83%) and the lowest fine-mode-volume median radius (0.145 μm). On the other hand, in a study about smoke plume characteristics in diverse BB regions over Asia, Vadrevu et al. [7] found out that forest fires had higher values of AAOD (absorption aerosol optical depth) and UVAI (UV aerosol index), compared with peat and agricultural fires. The burning intensity of the broadleaf forest (in Laos) is higher than the other vegetation fires. Thus, we can infer that the mixture of forest and peat leads to less BC (first study), while a pure forest (especially the broadleaf forest) smoke has the largest BC content (second study), and consequently higher absorbing aerosols.

Similar to Shi et al. [6], in a study over the US based on MISR and aircraft in situ data, Junghenn Noyes et al. [8] observed the following: near the source, the smoke particles contained fine, highly absorbing, BC-like aerosols, whereas downwind, they observed an increase in the fraction of weakly absorbing, less BC-like aerosols. In the same context, based on laboratory studies, Smith et al. [9] reported low SSA (high BC) for flaming combustion and higher SSA for smoldering combustion, while the aged smoke had the highest SSA. MISR data suggested an increase in size between ~30 and 140 min of aging, but decrease in size for smoke older than 140 min. The authors infer that VOC (volatile organic compound) condensation and possibly coagulation occur between ~30 and 140 min of aging, that gravitational settling and/or dilution alter vertically resolved particle size as the smoke ages beyond about 140 min, and particles on average become progressively more oxidized downwind along the entire plume.

Aircraft measurements in West Africa [10] showed that the fresh smoke is dominated by particles with a radius below 100 nm, while the aged smoke is dominated by particles with a radius between 100 nm and 200 nm. The number of condensation nuclei is around 10^4 cm^{-3} and 10^3 cm^{-3} for fresh and aged smoke, respectively.

A link between the optical properties measured by lidars and the potential aerosol sources was assessed in recent studies [11–13], based on the method developed by Radenz et al. [11], which tries to assess the air mass source attribution (based on land cover types or geographical regions) for specific heights in a lidar profile. The back-trajectories are computed for specific heights and a residence time is calculated as the ratio between the time spent by the air mass parcels below a certain reception height over different land cover types (water, savanna/shrubland, urban, barren, forest, grass/cropland, and snow/ice) or different geographical regions, and the total time of the back-trajectory. The residence time can be computed either for a mean trajectory or for an ensemble of back-trajectories. For this application, the nominal reception height is 2 km (following Val Martin [14]) and it is associated with the common PBL height. The attribution of the sources for various land cover types is made based on the residence time spent over those land cover types. For example, the lidar measurement at a certain altitude can have the air mass sources originating from grass, barren, and savannah. However, specific pollution events occurring over specific areas are not identified (e.g., biomass burning).

Amiridis et al. [15] found that the lidar ratio at 355 nm increases (while backscatter Ångström exponent at 532/355 decreases) with the age of CO (i.e., smoke's age), where the age varied from 6 days to 17 days. The BB events analyzed in their study were associated with agricultural fires. Furthermore, Amiridis et al. found that the optical characteristics of smoke aerosol were variable, and this behavior was mainly attributed to the fact that the burned regions were located at variable distances from the lidar station, and thus, the observed smoke had different aging properties. The CO emission, in turn, is proportional to the burned area, biomass per area, and CO emission factor, which is specific for different land cover types [15–17].

In a study about smoke plume characteristics in diverse BB regions over Asia, Vadrevu et al. [7] used CALIPSO (Cloud–Aerosol Lidar and Infrared Pathfinder Satellite Observations) data and determined vertically elevated aerosol profiles in the altitude range of 3.2–5.3 km for the forest fire plumes, compared to 2.2–3.9 km and less than 1 km in agriculture and peatland fires, respectively. Based on CALIPSO measurements in the region of active fires, Labonne et al. [18] reported injection heights up to 7 km. Val Martin et al. [19] analyzed satellite data for smoke injection heights from fires in North America for several biomes (land cover types) over five years. The highest plumes were observed for the boreal region (median ~850 m), whereas the lowest, smallest plumes were observed over cropland and grassland (median ~530 m). Amiridis et al. [20] estimated an empirical relationship between the smoke injection height and FRP (fire radiative power) for agricultural burning.

In order to assess high temporal and spatial resolution of aerosol measurements, the ground-based lidars are a valuable tool, in particular the EARLINET (European Aerosol Research Lidar Network; https://www.earlinet.org/ last access: 05 April 2022; e.g., [21]), which is part of the Aerosol Cloud and Trace Gases Research Infrastructure (ACTRIS) (https://actris.eu, last access: 5 April 2022). Most of the BB smoke studies from ground-based lidars over Europe focus mainly on the smoke's optical properties and some of them on the smoke's microphysical properties or its radiative impact (e.g., [22–24]). In these studies, BB smoke was labeled as fresh or aged using various criteria. Based on the intensive parameters CR_{LR} (color ratio of the lidar ratios) and EAE (extinction Ångström exponent), it was observed that in general the fresh smoke has $CR_{LR} < 1$ while EAE > 1.4 [25]. The aged smoke corresponds to long range transport (LRT) where the smoke is measured after a few days (e.g., [25–29]) of transportation or even after a week, as is the case for the BB smoke transported from North America (e.g., [22,23,30–35]). The smoke from strong wildfires can penetrate into the stratosphere and thus persist longer, while it can be transported over large distances (e.g., [23,33,36]). Many studies have reported a wide range of lidar BB optical properties as summarized by Adam et al. [37]. These properties are referred to mostly as lidar ratio (LR) at two different wavelengths 355 nm and 532 nm, EAE, and backscatter Ångström exponent (BAE). The main findings in [37] are shown in Table 1.

Table 1. Range of the smoke's optical properties in literature, based on the review in [37].

	LR355 [sr]	LR532 [sr]	EAE	BAE355/532	BAE532/1064
All events	21–130	26–147	0–2.4	0.35–2.8	0.29–2.85
Fresh smoke	40–114	30–100	0.87–2	0.58–1.8	0.39–1.32

Since the current studies on the optical properties of the transported smoke provide a quite high range in the measured parameters, our knowledge of the optical properties of smoke parameters of specific land cover types is not yet complete. This study aims to contribute towards a better understanding between the land cover (vegetation type) which fuels the BB and the optical properties measured by lidar (by means of the intensive parameters). Such information can be useful for smoke transport models to forecast the effect of various biomass burnings as well as to establish its specific radiative effect. Thus, the purpose of this study is to investigate the potential relationships between the land cover (vegetation type) which fuels the BB and the optical properties measured by lidar (by means of the intensive parameters). The study is organized as follows: Section 2 describes the materials and methods used in the current study; Section 3 presents the results and their discussion; and Section 4 summarizes the main conclusions.

2. Materials and Methods

In this study, observational datasets and numerical modeling data are used. More specifically, the materials involved in this research are the following: a multiwavelength Raman lidar, the Hybrid Single-Particle Lagrangian Integrated Trajectory (HYSPLIT) back-

trajectories, and the Terra and Aqua combined Moderate Resolution Imaging Spectroradiometer (MODIS) through the Fire Information for Resource Management System (FIRMS) and land cover. Additional information from FLEXPART (FLEXible PARTicle dispersion model) and ground in situ and photometer data are used (subject to availability). The following sub-sections provide a short description of the instruments and methods used for data analysis.

2.1. Multiwavelength Raman Lidar RALI

The measurements of the BB smoke obtained with a multiwavelength Raman lidar (RALI) during the period 2014–2017 operating in Măgurele, Romania (44.3448° N, 26.0123° E), were analyzed. RALI is part of EARLINET/ACTRIS infrastructure. RALI operates at three emitting wavelengths, 355 nm, 532 nm, and 1064 nm, and acquires the backscatter radiation elastically scattered as well as inelastically scattered at the N_2 Raman channels 387 nm and 607 nm. More details about the specific lidar system are available in Nemuc et al. [38]. The backscattered radiation at 532 nm is acquired by two channels representing the parallel polarized light (532 p) and cross-polarized light (532 s). All channels but 1064 nm use both analog and photon counting detection. Note that the 532 nm receiving channels are usually noisier, and part of this behavior may come from the fact that the output laser power is the smallest for 532 nm (~50 mJ). The low power also affects the detection efficiency at 607 nm.

The data were processed using Single Calculus Chain (SCC) [39–41], version 5.2.3. Six datasets (corresponding to six time stamps), quality controlled, ranging over the period 2014–2017, containing 11 lofted aerosol pollution layers, were selected. The datasets correspond to 3 backscattering + 2 extinctions. Following Adam et al. [37], the intensive parameters (IPs) are further used in data analysis. The data quality control (QC) closely follows the steps described in [37]. In summary, the criteria used for the data selection are the following: (a) visual inspection of all the profiles; profiles displaying atypical shape are dismissed, (b) profiles for which no significant layer is observed are dismissed, (c) the aerosol pollution layers are selected if there are at least 80% of the data in the layer for each of the optical properties (backscattering and extinction coefficients), (d) optical properties with SNR (signal to noise ratio) smaller than 2 are dismissed, (e) IPs' filtering, based on the literature for their typical range for BB smoke. Thus, all layers with IPs outside of the following limits were not considered for further analysis [37]: LR@355 = [20, 150] sr, LR@532 = [20, 150] sr, EAE = [−1, 3], BAE@355/532 = [−1, 3], and BAE@532/1064 = [−1, 3]. (f) IPs with SNR smaller than 2 are dismissed. The aerosol pollution layers were automatically determined using the algorithm described in [42]. The algorithm was used for both lidar profiles (signal = particle backscattering coefficient at 355 nm) and ceilometer profiles (signal = range corrected signal—RCS at 1064 nm) [43]. The main steps of the algorithm are: (1) calculate the variance of the cumulative signal (VCS), (2) define a new vector as NV = VCS(1:2:end-1) ∗ VCS(2:2:end) where the indexing 1:2:end-1 (2:2:end) is the mean from the first index to the penultimate index with the step of 2 (from the second index to the last index with the step of 2), (3) find the local minima in NV (which corresponds to the location of the minima and maxima in the signal) and the local maxima in NV (which gives the location of the inflection points in the signal). A few other criteria are involved in order to select the layers, such as the prominence of the inflection points. The algorithm is written in Matlab where the functions islocalmax and islocalmin are used [44].

The IPs are: LR at 355 nm and 532 nm, EAE between 355 nm and 532 nm, backscattering Ångström exponent (BAE) between 355 nm and 532 nm and between 532 nm and 1064 nm. Recall that the IPs are independent of the aerosol load and are solely aerosol-type-dependent. Conversely, the extensive parameters (aerosol backscatter and extinction coefficients) are related to the aerosol load.

2.2. HYSPLIT Back-Trajectory and ERA5 Reanalysis

The HYSPLIT model (see [45,46] and their citations) is widely used to assess the air mass origin and thus the sources of the aerosol pollutants. In the lidar community, the assessment of an air mass origin is based in general on a single back-trajectory run of HYSPLIT, from the point of interest backwards (e.g., [37,43]). However, there are several studies which use the HYSPLIT ensemble trajectories in order to increase the confidence that the vast majority of the air parcels arriving in a location come from the same region (likely pathways) (e.g., [12,32,47–51]). The HYSPLIT ensemble trajectories use 27 trajectories corresponding to slightly different meteorological input (by changing the grid factor with offsets on longitude, latitude, and altitude). Sometimes, a small number of trajectories are used to show consistency of the air passage over a region [31]. Another approach to estimate the consistency of the air mass origin is to verify each trajectory against its reverse trajectory, running the model in the opposite direction to assess the integration error. Then, pairs of backward and forward trajectories with a relative error (distance between the ending point of the backward trajectory and the starting point of the forward trajectory with respect to the total travel distance) lower than 5% are considered [52].

The present method considers a slightly different approach. The aerosol pollution layer is divided in at least 30 levels and for each level, a back-trajectory is run. The range resolution (multiple of 5) varies from 15 m to 60 m (depending on the layer's depth). The HYSPLIT model was initially run backward in time for 240 h with a 1 h time step starting at the time the layer was detected. Based on trajectories analyses, its uncertainty towards long distance and fires' locations, we re-run the back-trajectories for shorter times (from 1 day to 4 days). The Global Data Assimilation System (GDAS) $1^\circ \times 1^\circ$ gridded meteorological data from the NOAA's Air Resources Laboratory [53] is used to drive the model. Within the next step, the mean trajectory is computed using the Cluster Analysis tool from HYSPLIT (which requires as input at least 30 trajectories). The meteorological field over the mean trajectory is also extracted from GDAS1 (corresponding to the geographical locations) using the ARLreader python library [54].

In addition, to increase the confidence of the mean trajectories obtained, we analyzed the meteorological fields provided by ERA5 reanalysis. ERA5 is based on the Integrated Forecasting System (IFS) Cy41r2, providing meteorological data at a high temporal (hourly) and horizontal ($0.25^\circ \times 0.25^\circ$) resolution, and 137 vertical levels spanning from the Earth's surface to 0.01 hPa [55]. For each mean backward trajectory, we chose the closest geopotential height to the measurement altitude and generated the composite map based on the time frame between the moment the last fire source was detected and the moment of the lidar measurement. Thus, the geopotential composite maps can be used as "proxy/cross-check data" for air mass circulation providing information on the general (average) state of the atmosphere during the BB aerosols' transport towards the measurement site. The parallel use of models that incorporates GDAS data and ERA5 reanalysis data were previously used in various applications (e.g., the evaluation of precipitation patterns [56], surface wind speed [57]).

2.3. MODIS FIRMS

MODIS FIRMS [58] contains the inventory of the fires. We assume that a fire contributes to the smoke transport if it is within $\pm$100 km around the mean air mass trajectory and within $\pm$1 h from the air mass passage [37]. We calculated the injection height following the empirical formula of Amiridis et al. [20], which was obtained from a regression analysis between the injection height as retrieved from CALIPSO (Cloud-Aerosol Lidar and Infrared Pathfinder Satellite Observations) measurements and the *FRP*. Thus, the injection height (I_h) is calculated based on *FRP*:

$$I_h = 10^{2.94} FRP^{0.39} \text{ [m]} \quad (1)$$

Amiridis et al. [20] studied fires which occurred in Eastern Europe over agricultural land and the values of the injection height ranged between 1.6 km and 5.9 km.

The fires with an injection height below the altitude of the air mass were dismissed. In addition, when available, we gathered the *APT* (altitude of plume top a.s.l.) from the CAMS (Copernicus Atmosphere Monitoring Service) Global Fire Assimilation System (GFAS) [59,60]. The GFAS assimilates *FRP* observations from NASA Terra MODIS and Aqua MODIS [61] sensors to produce daily estimates of biomass burning emissions with a resolution of $1^\circ \times 1^\circ$. It has been extended (GFAS v1.2) to include information about injection heights derived from fire observations [62] and meteorological information from the operational weather forecasts of ECMWF [63]. The GFAS data are available at https://apps.ecmwf.int/datasets/data/cams-gfas/ (accessed on 12 July 2022).

2.4. MODIS Land Cover

The MODIS land cover products MCD12C1 [64] were used to extract 11 types of vegetation. According to [64], the MODIS Land Cover Climate Modeling Grid (MCD12C1) Version 6 data product provides maps of the International Geosphere-Biosphere Program, University of Maryland, and Leaf Area Index (LAI) classification schemes at yearly intervals at 0.05 degree (5600 m) spatial resolution for the entire globe from 2001 to 2019. Sub-pixel proportions of each land cover class in each 0.05-degree pixel are provided along with the quality assessment information for each of the three land classification schemes. The 11 vegetation types/layers ('Land_Cover_Type_3_Percent') are shown in Table 2. The data provide percentages for each LAI class at each pixel. We looked for the data over the range of $[15^\circ, 70^\circ]$ latitude and $[-115^\circ, 65^\circ]$ longitude (as this usually covers the 10-day back-trajectories from our site).

Table 2. Vegetation types (land cover) [64] and their associated numbering (roman numbers) that are used in this study.

#	I	II	III	IV	V	VI	VII	VIII	IX	X	XI
Vegetation type	water	grasses or cereal	shrubs	broadleaf crops	savannah	evergreen broadleaf forest	deciduous broadleaf forest	evergreen needleleaf forest	deciduous needleleaf forest	unvegetated	urban

For each smoke layer detected by lidar measurements, we extracted the land cover associated with the fires contributing to the smoke layers. The number of fires contributing to the smoke layers differs from case to case. The predominant vegetation type (*PVT*) for each fire was assigned for the vegetation type with the largest contribution in the pixel (in percentages). When more fires contribute to the smoke layer, an effective *PVT* (*EPVT*) is calculated. In these situations, we handle a mixed smoke layer. The *EPVT* is defined as the *PVT* which contributes the most to the total smoke emission rate. For each fire, we extracted the emission coefficient C_e (in kg MJ^{-1}) [65] (1° spatial resolution) and then we computed the rate of the smoke emission (in kg s^{-1}) as [65]:

$$R_{sa} = C_e FRP \, [\mathrm{kg/s}] \quad (2)$$

Note that for the calculation of the total emission rate, some fires may contribute twice (due to the air mass low motion in the area) and thus we account for this aspect.

2.5. Additional Data/Information

2.5.1. FLEXPART

FLEXPART is a particle dispersion model designed to compute the long-range transport, considering the diffusion and the dry and the wet deposition of particles. FLEXPART

outputs are suitable for inverse determination of emission aerosol sources, such as greenhouse gases, dust, smoke, haze, or volcanic ash. The input data are 3-D meteorological fields retrieved from the ECMWF (European Centre for Medium Range Weather Forecasts) or GFS (Global Forecast System). The model solves the equations for transport, turbulent diffusions, and other relevant processes in a Lagrangian framework [66]. FLEXPART can run in forward mode or backward mode. In forward mode, it simulates the transport and dispersion of emissions from given sources towards receptor points, producing gridded output concentration and deposition. In backward mode, it produces the source–receptor relationship with respect to a point source or gridded sources for given receptors [67]. Source–receptor relationships describe the sensitivity of the concentration at a receptor site to emission sources. Source–receptor sensitivities (kg^{-1} s) can be multiplied with source–strengths derived from an emission inventory (kg s^{-1}), yielding a dimensionless mass mixing ratio at the receptor [67].

In this study, the FLEXPART version 10 [68] is used. The meteorological data used as input were obtained from the ECMWF global meteorological fields with a horizontal resolution of 0.5° × 0.5°, a temporal resolution of one hour, and using the lowest 70 vertical levels (corresponding to pressure levels from surface to 150 hPa) out of the 137 vertical levels. The transport of aerosols (and source–receptor sensitivity—SRS) for each layer identified from lidar measurements was simulated considering all atmospheric processes (e.g., cloud, wet and dry deposition, aging, turbulent diffusion) starting with 10,000 particles tracked for one up to four backward days (24–96 h), with the particle positions being stored every hour. Black carbon was used as tracer and start time of the simulations was given by the time at which the aerosol layers from the biomass burning were observed. The black carbon and organic carbon were extracted from the global emission inventory GFED 4 [69]. SRS describes the potential of the emission sources to contribute to the receptor concentration. SRS is presented as a pattern (on a grid with a resolution of 0.2 × 0.2, on a scale of 0–1) on the FLEXPART output grid, in relative units. Combining the residence time obtained from FLEXPART with emissions of black carbon and organic carbon, the contributions of biomass burning emissions from eight types of BB were computed. The main contributors to the BB smoke are: (1) agricultural waste burning, (2) savanna, grassland, and shrubland fires, and (3) temperate forest fires.

The same parametrization of biomass injection height [20] was used to calculate the biomass burning concentrations recorded at the receptor.

2.5.2. Photometer

In this study, we used data from two different photometers (part of AERONET) operating in the same location with the RALI system. The first one covers the period 2014–May 2015 and the second one the period May 2015–2018. The sun photometer measurements started in 2007 with the installation of a sun/sky CIMEL Electronique 318A (station ID: "Bucharest_INOE"). In 2015, a new Cimel CE318-T (referred as C318T) sun/sky/lunar (triple) photometer was installed at INOE, replacing the older sun/sky CIMEL Electronique 318A photometer. Thus, a new AERONET [70] station (ID: "Magurele_INOE") has been developed since then, complementary to the previous one (ID: "Bucharest_INOE"). A description of the history of the station at Măgurele and the photometers operating there is given in previous studies [43,71]. The photometer performs spectral measurements of the direct sun/lunar irradiance and the sky radiance in the almucantar and principal plane configurations at 10 nominal wavelengths of 1020, 937, 870, 675, 500, 440, 380, and 340 nm, using a silicon photodiode detector, as well as additional measurements at 1020 and 1640 nm using an InGaAs (indium gallium arsenide) detector [72]. The aerosol optical depth (AOD) can be obtained from the direct sun observations through the Beer–Lambert law [73] and can be used for the estimation of the aerosol size (Ångström exponent—AE) using the Ångström parameter relationship, while the fine-mode (FMAOD), and coarse-mode (CMAOD) AOD at 500 nm and fine-mode fraction (FMF) are retrieved using the spectral de-convolution (SDA) algorithm [74]. In the current study, we used the AE and

FMF cloud-screened and quality assured Level 2 Version 3 [75] values obtained from the photometer measurements.

2.5.3. Ground-Based In Situ Data

A multiwavelength aethalometer (370, 470, 520, 590, 660, 880, and 950 nm; AE33, Aerosol d.o.o, Slovenia) was used to quantify equivalent black carbon (BC) mass concentrations. The separation between BC resulting from biomass burning (BCbb) from that resulting from fossil fuel (BCff) was conducted based on the approach described in [76]. We considered the maximum concentration period of BC_{bb} as the time period when the average concentration (computed 24 h after the beginning of the lidar measurement) is exceeded.

2.6. Methodology

The diagram with the steps undertaken in the current methodology is shown in Figure 1. We selected the smoke layers (step 3) as those layers for which there were fires along the mean back-trajectory (within ±100 km and within ±1 h from the passage of the air mass). Only the fires for which the injection height was higher than the air mass altitude were selected. A total of 6 time stamps (with 11 smoke layers) were identified.

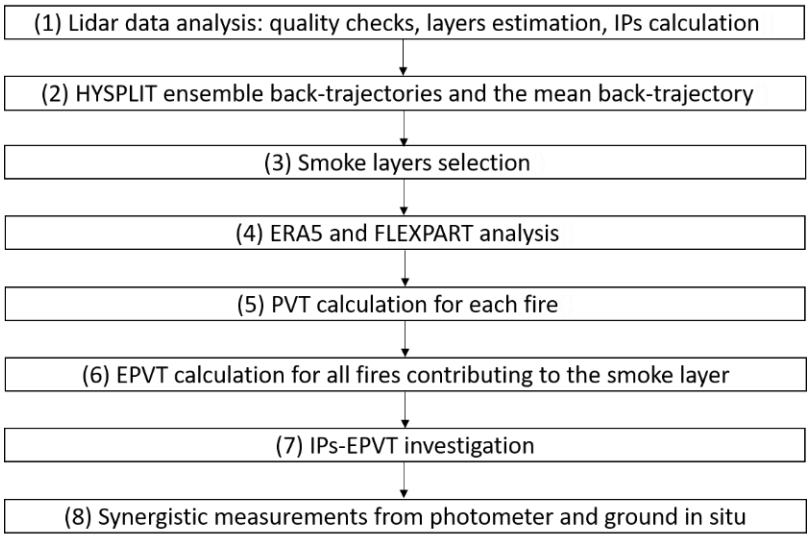

Figure 1. Methodology diagram.

In addition, the ERA5 reanalysis was performed to determine the mean air flow while the FLEXPART source–receptor sensitivity was employed to assess the potential BB sources to the smoke measurement (step 4).

3. Results and Discussions

In Section 3.1 we discuss a case study (25 July 2016) to illustrate the methodology, while in the next section we investigate all the results. The case study is representative for 3 out of 11 cases where the air mass circulation comes from the north of Romania.

3.1. Case Study 25 July 2016

The following analysis is based on the intensive parameters LR, EAE, and BAE.

During 25 July 2016 we measured on consecutive hours two layers above the planetary boundary layer. For the first measurement, between ~17:30–18:30, one layer was detected spanning from 1830 m to 3510 m a.g.l., while the next hour two layers were identified, between 930 m and 2070 m a.g.l. and between 2190 m and 3390 m a.g.l. Figure 2 shows the averaged lidar profile during the second hour. The corresponding values of the IPs for both hours are given in Table 3. The lower smoke layer identified in the second hour of measurements has the major contribution from vegetation type IV (broadleaf crops)

while the upper layer (identified in both hours) has a major contribution from vegetation type II (grasses or cereals). The fires contributing to both layers are different, as seen by their location (see Figure 3, Figures S6 and S7 in the Supplementary Materials). There are two contributing fires to the upper layer, located in northeast Romania and south Ukraine (see Figures S6 and S7). In addition, a third fire, located close to the measurement site, is observed for the second hour of measurements. The travel time corresponding to the fire which contributed the most (south Ukraine) is ~26 h and ~27 h for both measurements. The lower layer has nine contributing fires (see Figures 3–5) and the median travel time from the fires contributing the most (which gives EPVT) is ~32 h. According to CR_{LR} and EAE values, the lower smoke layer was labeled as fresh smoke, as well as the upper layer in first hour of measurements (as shown later in Section 3.2.2). However, the upper layer was labeled as aged in the second hour of measurements, which is surprising. This case needs further investigation.

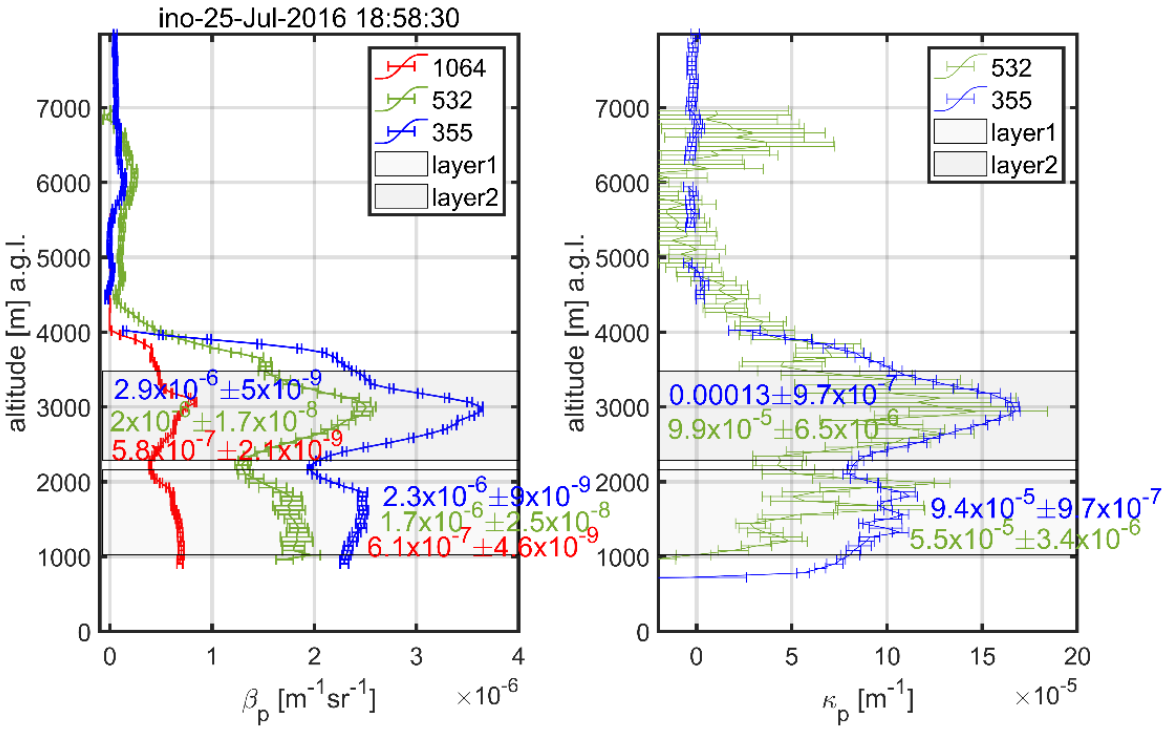

Figure 2. Lidar averaged profiles over ~18:30–19:30 UTC on 25 July 2016: aerosol backscatter coefficient at 355 nm, 532 nm, and 1064 nm (**left**) and aerosol extinction coefficient at 355 nm and 532 nm (**right**). The layers are marked (gray shaded) while the mean values of the optical properties in the layer are shown with the corresponding color for each parameter.

Table 3. Intensive parameters for smoke layers detected on 25 July 2016, along with the associated burned land cover type (EPVT). Layer represents the mean layer altitude.

Lidar Time UTC	Layer [m] a.g.l.	LR355 [sr]	LR532 [sr]	CRLR	EAE 355/532	BAE 355/532	BAE 532/1064	EPVT
~17:30–18:30	2670	43 ± 0.4	34 ± 3.1	0.8 ± 0.1	1.65 ± 0.22	1.11 ± 0.03	1.64 ± 0.02	II
~18:30–19:30	1500	40 ± 0.4	32 ± 2.1	0.8 ± 0.1	1.34 ± 0.16	0.79 ± 0.04	1.48 ± 0.02	IV
	2790	45 ± 0.3	50 ± 3.3	1.1 ± 0.1	0.72 ± 0.16	0.99 ± 0.02	1.76 ± 0.01	II

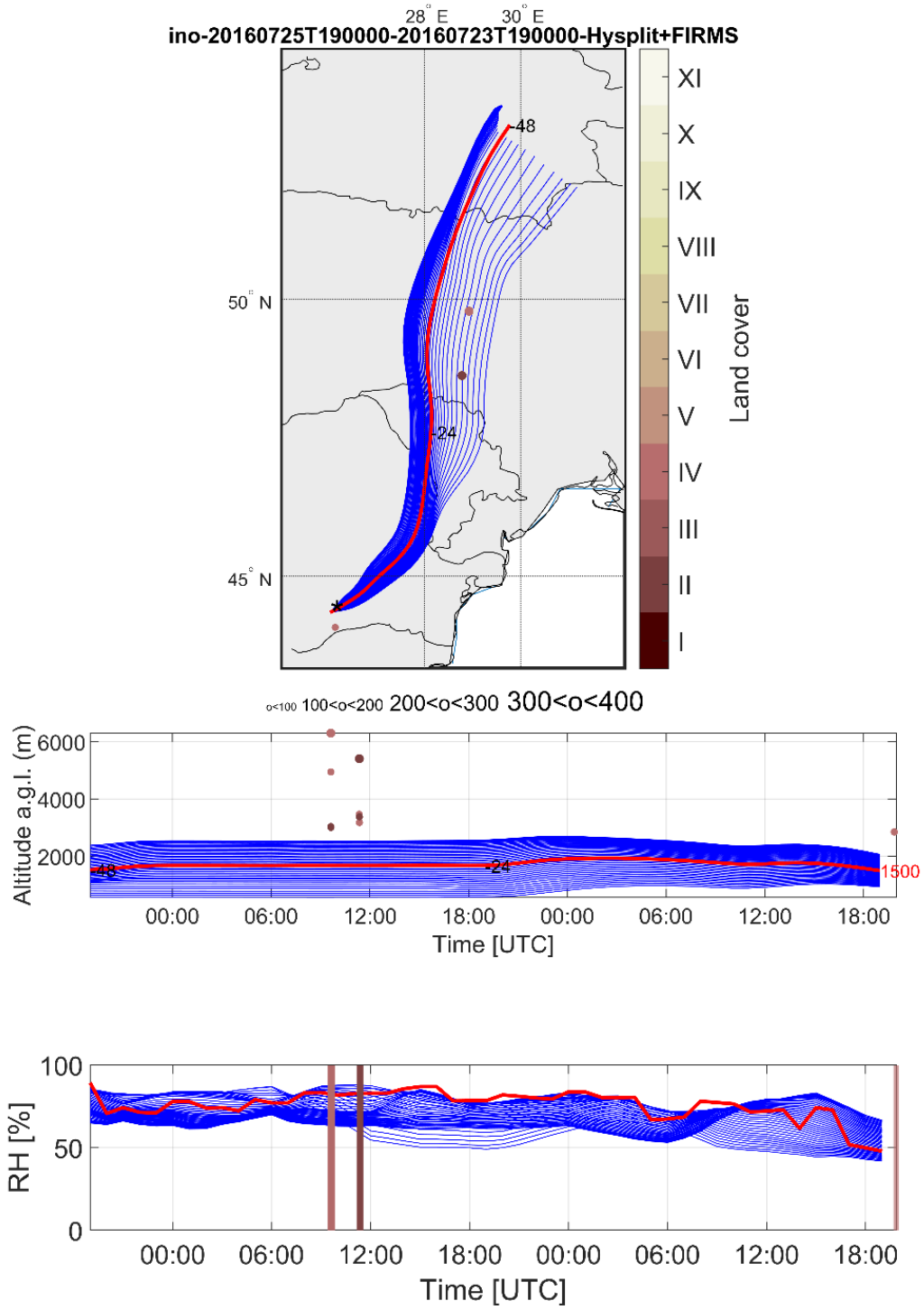

Figure 3. Ensemble back-trajectories (blue lines) and the mean trajectory (red) for 25 July 2016 19:00 UTC. The middle plot shows the trajectory altitudes versus time. The brown dots represent the fires' locations (**upper plot**) and their injection height (**middle plot**). The smoke middle layer is at 1500 m a.g.l. The **lower plot** shows RH for both ensemble and mean trajectories. The location of the fires is shown by bars. Note that the fires' colors represent the land cover type (legend **upper plot**), while their dimensions are set up according to their FRP size in MW (upper plot, x−label).

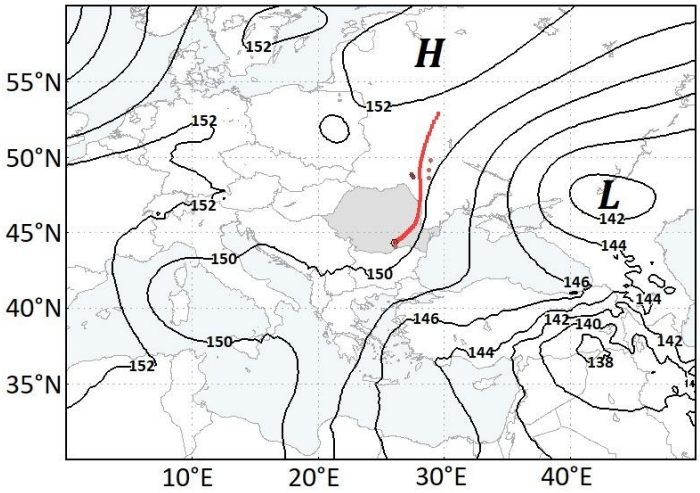

Figure 4. ERA5 reanalysis of mean geopotential height at 850 hPa (black contours) during 24 July 2016 00UTC and 25 July 2016 19UTC. The mean trajectory (red) is overlapped, and the fires are shown in brown dots (similar with Figure 2).

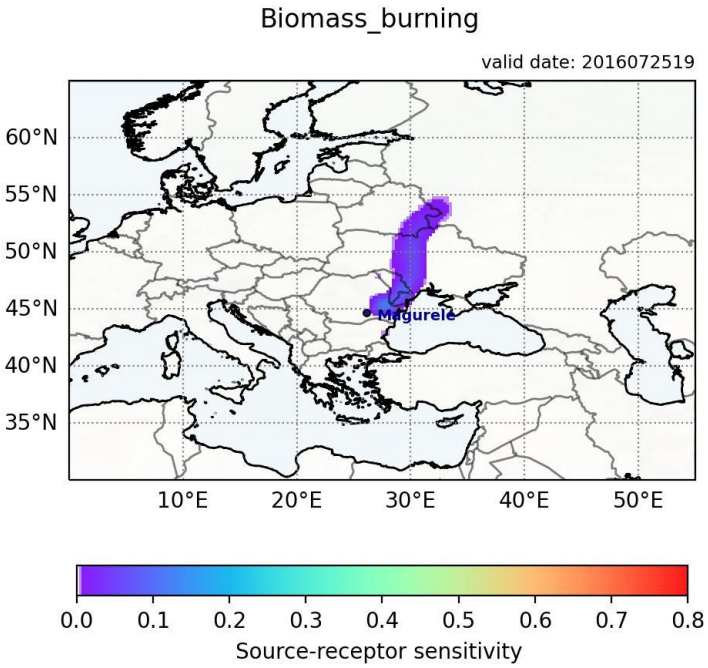

Figure 5. FLEXPART source–receptor sensitivity for the lidar measurement on 25 July 2016 19:00 at ~1500 m.

Figure 3 shows an example of the ensemble back-trajectories and the mean back-trajectory along with the location of the fires. Figure 4 details the synoptic context over the region of interest, including the location of the measurement site and the fires' sources, in terms of mean geopotential height at the closest level to the altitude at the measurement site. The geopotential height map at 850 hPa (corresponding to ~1500 m altitude) is the composite over the first 43 h of the back-trajectory. The selection of the time interval for the composite was based on the fact that the fires were detected in the first 43 h. During this time frame, we observe that the atmospheric regime over the area of interest is dominated by a high-pressure system, which enables the northeast–southwest displacement of the air mass. The overlapped mean trajectory (red contour) follows the height contour of 150 gpdam, indicating that the air mass displacement crosses the area where fires were located in Ukraine and the travel time is less than two days. The CAMS retrievals for the

altitude (a.s.l.) of the plume top (APT) provide the value of 1818 m a.s.l. for 24 July 2016 09:38 and 11:22 UTC. For these times, the empirical formula employed here to compute the injection height provides higher values (from 3008 m a.g.l. and 6305 m a.g.l., with the terrain altitude of 290 m). Although there are differences between the injection height determined in CAMS and the empirical formula, the actual altitude of the air mass was below both retrievals. This feature was observed for all the cases that CAMS APT retrievals were available.

The source–receptor sensitivity (Figure 5) as processed using FLEXPART [67] shows potential sources for BB on a [0 1] scale, in agreement with the HYSPLIT coverage. The highest contribution (97%) is provided by agricultural waste.

The Ångström exponent (AE440/675) provided by a photometer was 1.46, while the fine-mode fraction (FMF) was 0.94 at about 16:54 UTC, which were the closest photometer retrievals to the lidar profiles. The daily average values of AE440/675 and FMF were 1.49 ± 0.03 (1σ) and 0.94 ± 0.009 (1σ), respectively. These values show that the aerosol was dominated by fine particles during the whole day. The black carbon (BC) measured at ground level was investigated for the next 24 h after the smoke layer measurement. The maximum concentration of BC from biomass burning was 29.37%, recorded between 19:43 and 00:04, while the corresponding total BC concentration was 2.24 μg m^{-3}. The total BC concentration is similar to values obtained for other sites in Europe during summer [77], while the BC from biomass burning fraction takes values from 5 to 37% for urban background and rural area affected by biomass burning, respectively.

3.2. Overview of All 11 Layers

For the 11 smoke layers selected, based on the location of the fires along the main HYSPLIT back-trajectory, the ensemble back-trajectories converge (i.e., the mean trajectory has a high level of confidence over the time period the fires were detected). The ERA5 reanalysis confirms the main flow. Except one case (10 July 2017), SRS plots by FLEXPART are in agreement with the main flow and thus they show the BB contribution to our measurements. The HYSPLIT, ERA5, and FLEXPART plots for the remaining ten cases are shown in the Supplementary Materials (Figures S1–S10). The corresponding lidar profiles for backscatter and extinction coefficients are shown in Figures S11–S15.

The following statistics were calculated over 11 layers (corresponding to six time stamps). Note that four measurements are consecutive (two by two), and thus, we have four events recorded.

The air mass circulation for the analyzed cases were from the east–northeast direction (five cases—Figures S1–S5) and from the northern direction (three cases—Figures S6 and S7, Figures 3–5), enabling the transport of biomass burning from Eastern and Northern Ukraine. In one case (10 July 2017), the circulation was from the west–northwest direction, allowing the local transport of BB (from southwestern and western Romanian regions). For this particular case, the FLEXPART source–receptor sensitivity shows an area located northeasterly and thus partly in disagreement with HYSPLIT and ERA5 (see Figure S8). A particular air mass circulation type is the one detected for the two layers on 7 August 2017. Following the high-pressure nucleus centered over Romanian territory, the airflow followed the clockwise circulation, initially from Central towards Eastern Europe, and then from Eastern towards Southeastern Europe, enabling the transport of BB from Eastern Ukraine (Figures S9 and S10).

FLEXPART analysis shows on one hand that the largest contribution to BB comes from agricultural crops (ranging from 74% to 99%). On the other hand, the contribution of the agricultural BB to the total sources contributing to the mass concentration ranges between 72% and 83%.

In addition, to exclude a possible dust contamination in the layers we analyzed the dust forecast (https://ess.bsc.es/bsc-dust-daily-forecast (accessed on 12 July 2022)) for our six measurements, which showed the following. For the first two lidar measurements (7 August 2014), the forecast did not show any dust intrusion over the region covered by the

back-trajectories. For the next two measurements (25 July 2016), the forecast showed some dust contamination over Central Europe. However, the back-trajectories did not approach the contaminated area, as they were originated from the northeast (Figures 3–5). For the fifth measurement on 10 July 2017, the dust forecast showed an extensive contamination over our region. We investigated the dust concentration profile, which showed some contamination over the ~2–6 km altitude region. Our investigated layer ranged over 1230 and 2190 m. As seen in the lidar profile (Figure S14), the profiles show indeed a layer over 2–6 km (not considered for our study). For the last measurement (7 August 2017), the dust forecast showed a small reminiscence of a previous dust event located westward from our back-trajectories.

3.2.1. Fires' Features

A total of 247 fires for which the injection height was above the air mass altitude were found along the 11 mean back-trajectories. The median of the travel time for all the smoke is 2.29 days. The maximum is 3.42 days, while the minimum is within the first hour of the back-trajectory, since the fire location was very close to the measurement's site. The travel times for the smoke corresponding to each of the vegetation types found are shown in Table 4. The vegetation type at the location of the fires is shown in Figure 6. We observe that most of the fires occur over the land with vegetation type IV (broadleaf crops). The other types found are type II (grass/cereals), type V (savannah), and type VII (deciduous broadleaf forest). The number of the fires for each vegetation type is shown in Table 4, while the caption of Figure 6 shows the percentages.

Table 4. Median, minimum, and maximum values for the travel time (in days) of the smoke for each of the land cover types found. The number of fires for each vegetation type is shown in parentheses.

Vegetation Type	Median	Minimum	Maximum
II—Grass/cereals (38)	1.29	0.25	3.4
IV—Broadleaf crops (196)	2.29	1/24	2.46
V—Savannah (9)	2.92	2.42	3.42
VII—Deciduous broadleaf forest (4)	3.4	3.4	3.4
Overall (247)	2.29	1/24	3.42

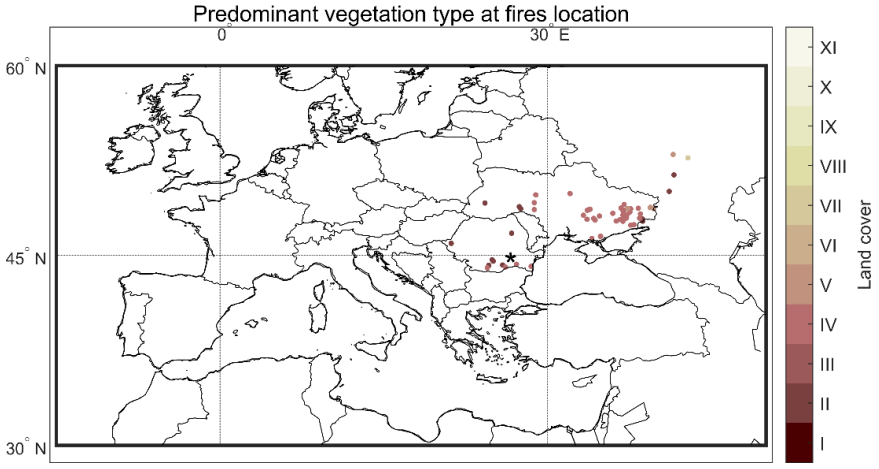

Figure 6. The vegetation type (land cover) at the fires' location. The numbers for land cover correspond to: I—water (0%), II—grasses or cereal (15.4%), III—shrubs (0%), IV—broadleaf crops (79.4%), V—savannah (3.6%), VI—evergreen broadleaf forest (0%), VII—deciduous broadleaf forest (1.6%), VIII—evergreen needleleaf forest (0%), IX—deciduous needleleaf forest (0%), X—unvegetated (0%), XI—urban (0%). The lidar measurement site is shown by a black star.

3.2.2. Intensive Parameters Versus Land Cover

For the 11 layers analyzed, EPVT was type II (grasses/cereal) for two smoke layers and type IV (broadleaf crops) for nine smoke layers. The IPs for both EPVT are shown in Figure 7. Broadly speaking, both types can be regarded as agricultural crops.

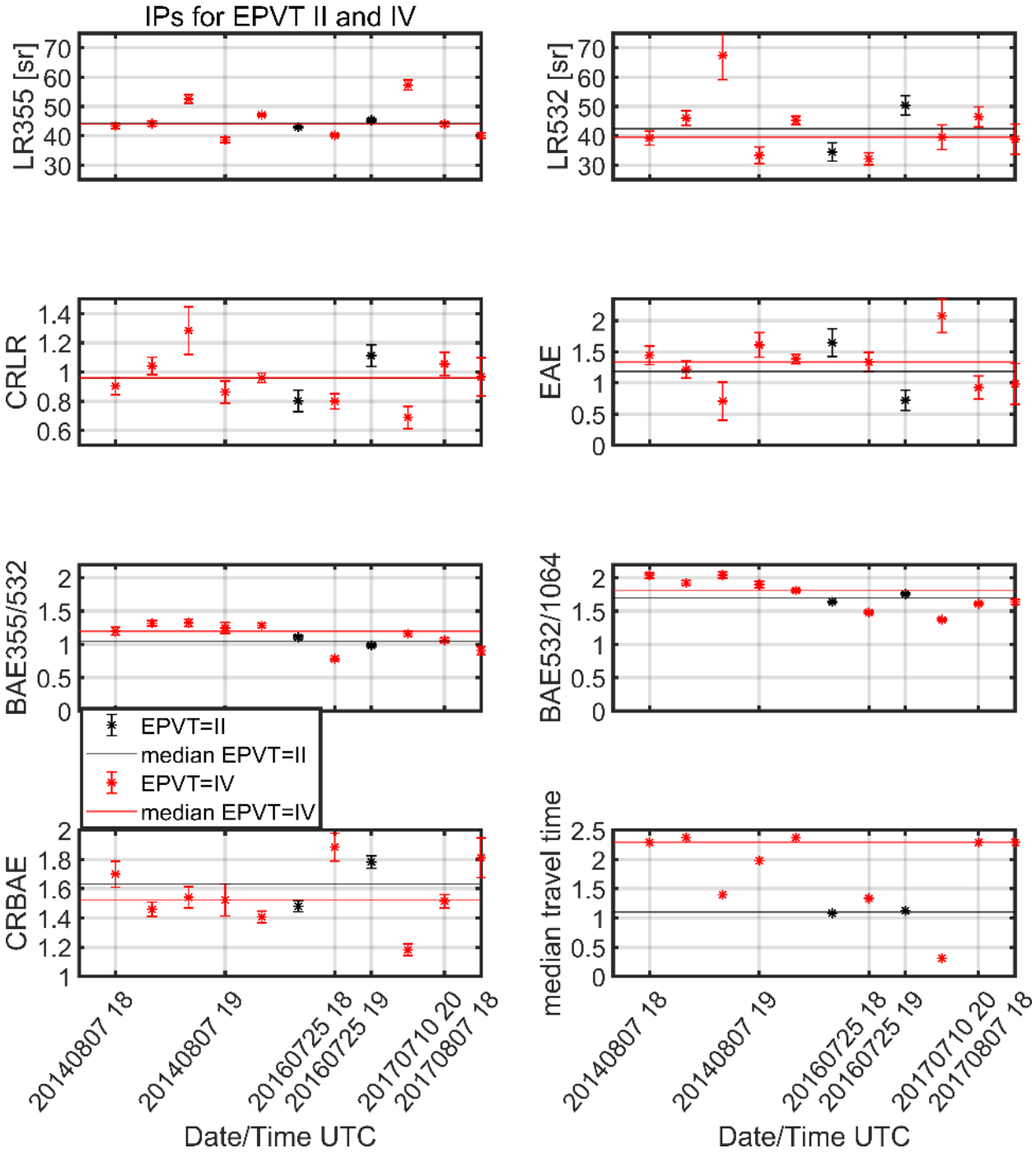

Figure 7. Intensive parameters for EPVT = II and EPVT = IV. Lower right plot shows the travel time for both types.

The median, minimum, and maximum values of the IPs are shown in Table 5. The median for type II does not indicate much, as we have two values only.

Table 5. Intensive parameters for EPVT II and IV.

	LR 355	LR 532	BAE 355/532	BAE 532/1064	CRLR	EAE	CRBAE	Travel Time (Days)
EPVT = II (grasses/cereal)—2 cases								
median	44.12	42.44	1.05	1.70	0.96	1.19	1.63	1.10
min	42.95	34.49	0.99	1.64	0.80	0.72	1.48	1.08
max	45.30	50.40	1.11	1.76	1.11	1.65	1.78	1.13
EPVT = IV (broadleaf crops)—9 cases								
median	44.00	39.53	1.20	1.81	0.96	1.34	1.52	2.29
min	38.59	32.13	0.79	1.37	0.69	0.71	1.18	0.31
max	57.32	67.45	1.32	2.04	1.28	2.08	1.88	2.4

The IPs are similar for both vegetation types. A larger number of events is required to draw significant differences or signatures. If we plot the IPs versus smoke travel time, we observe some trends. However, the correlation coefficients and their statistical significance are not high. For illustration purposes, we show these trends in Figure 8. Thus, we observe that LR355 and EAE tend to decrease with travel time while CR_{LR}, BAE, and CR_{BAE} tend to increase with travel time. The increase in CR_{LR} and decrease in EAE with smoke travel time is a characteristic for aged smoke [25,78]. In the current study, LR355 increases with BAE355/532. Thus, for this study, where the travel time is less than 3 days, the correlations for LR355 and BAE355/532 are opposite of those reported by Amiridis et al. [15], where the age of carbon monoxide (~travel time) is much larger (>6 days).

In order to assess the smoke characteristic (fresh versus aged), we make use of the EAE and CR_{LR} values. It was shown [25] that in general, the fresh smoke is characterized by EAE > 1.4 and CR_{LR} < 1. Figure 9 shows the relationship between the two IPs. The EAE and CR_{LR} values align themselves within error bars in the fresh (yellow corner) and aged smoke (dark green corner) categories as defined by both IPs. The travel time values (median, minimum, and maximum) for fresh smoke are: 1.65, 0.31, and 2.4 days. For the aged smoke, we have 2.3, 1.1, and 2.4 days, respectively. While the median travel time is smaller for fresh smoke (1.65 days) as compared with aged smoke (2.3 days), we observe that the maximum travel time observed for fresh smoke was 2.4 days while the minimum travel time observed for aged smoke was 1.1 days. Thus, we can conclude that the travel time alone cannot always label the smoke as fresh or aged. We observe that one smoke measurement associated with land cover type II belongs to fresh smoke, while the other one belongs to aged smoke. Five out of nine smoke measurements associated with land cover type IV represent fresh smoke. To a closer extent, we may label the event with travel time ~2.4 days and EAE = 1.39 and CR_{LR} = 0.96 as a mixture of fresh and aged smoke, as the values are very close to the thresholds.

The synthetized synergistic information regarding all the cases is shown in Table 6. The first observation is that the measurements were taken during sunset (see back-trajectory start time between 18:00 and 20:00 UTC).

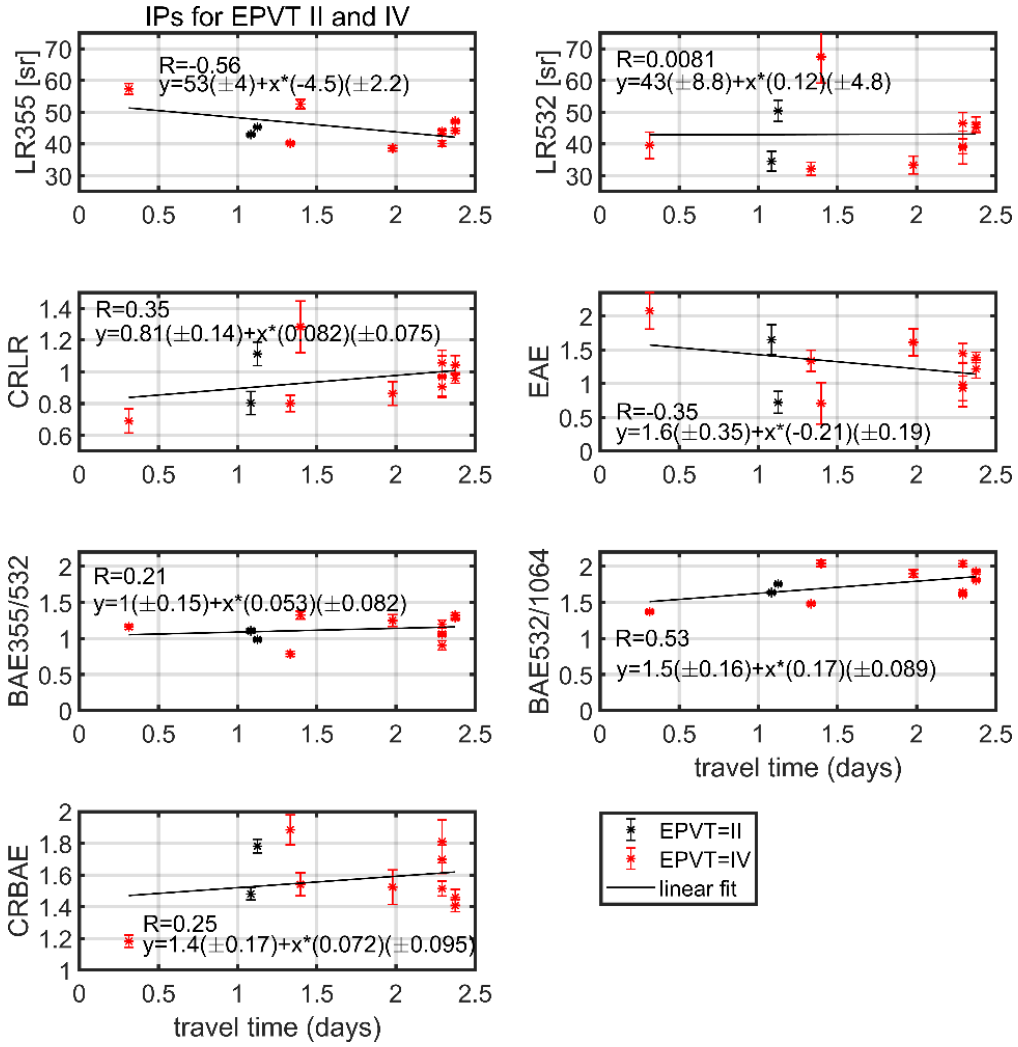

Figure 8. Intensive parameters versus smoke travel time.

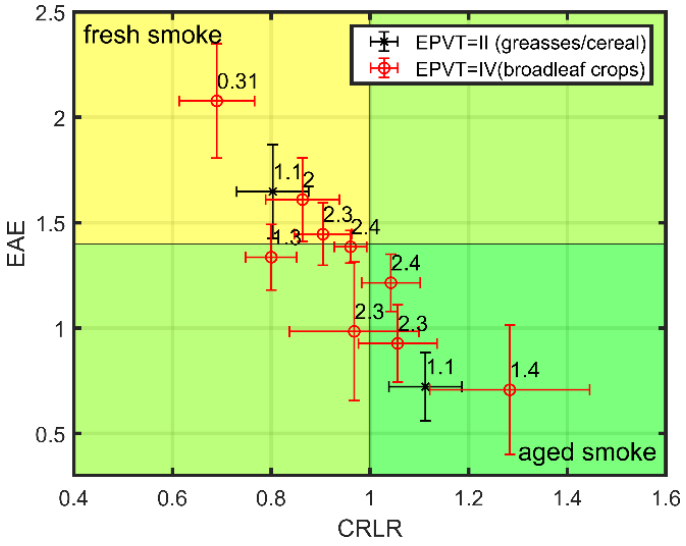

Figure 9. EAE versus CR_{LR}. The upper left corner shows typical values for fresh smoke, while the lower right corner shows typical values for aged smoke. The number represents the travel time in days.

Table 6. The main features for the 11 smoke layers. The fresh smoke is highlighted in light blue and the aged smoke in darker blue.

Date	20140807	20140807	20140807	20140807	20140807	20160725	20160725	20160725	20170710	20170807	20170807
time start back-trajectory	18	18	18	19	19	18	19	19	20	18	18
layer bottom agl [m]	930	1830	2910	930	1590	1830	930	2190	1230	1950	3030
layer top agl [m]	1705	2790	3390	1470	3270	3510	2070	3390	2190	2910	3750
layer mean altitude agl [m]	1318	2310	3150	1200	2430	2670	1500	2790	1710	2430	3390
extinction 532 [1/m]	1.10E-04	7.90E-05	8.70E-05	8.30E-05	9.60E-05	5.70E-05	5.50E-05	9.90E-05	4.23E-05	9.20E-05	4.10E-05
σ extinction [1/m]	6.10E-06	4.10E-06	1.10E-05	6.40E-06	2.80E-06	5.10E-06	3.40E-06	6.50E-06	4.47E-06	6.70E-06	5.40E-06
mass conc. [$\mu g/m^3$]	**29.21**	**20.98**	**23.10**	**22.04**	**25.49**	**15.13**	**14.60**	**26.28**	**11.23**	**24.43**	**10.89**
σ mass conc. [$\mu g/m^3$]	6.61	4.73	5.85	5.13	5.64	3.59	3.33	6.02	2.74	5.65	2.79
mass conc. agric. FLEXPART [$\mu g/m^3$]	**23.68**	**17.08**	**22.35**	**24.25**	**19.86**	**15.07**	**21.62**	**23.97**	**12.25**	**13.72**	**7.90**
STD mass conc. agric. FLEXPART [$\mu g/m^3$]	2.4E-02	1.7E-02	2.9E-02	2.4E-02	3.2E-02	1.3E-02	1.6E-02	2.2E-02	1.3E-02	7.8E-03	5.0E-03
# fires	5	**35**	3	4	**26**	2	9	3	4	**26**	**19**
# detections	9	60	4	6	49	4	15	5	6	52	37
Rsa	4.00	**29.77**	3.54	2.88	**24.68**	6.82	**23.34**	7.09	3.20	**77.65**	**47.97**
<travel time> [days]	2.29	2.38	1.40	1.98	2.38	1.08	1.33	1.12	0.31	2.29	2.29
EPVT	IV	IV	IV	IV	IV	II	IV	II	IV	IV	IV
LR355 [sr]	43.35	44.16	52.56	38.59	47.10	42.95	40.15	45.30	57.32	44.00	40.09
σLR355 [sr]	0.89	0.85	1.49	0.86	0.52	0.35	0.44	0.34	1.70	0.71	0.94
LR532 [sr]	39.23	46.04	67.45	33.32	45.25	34.49	32.13	50.40	39.53	46.47	38.81
σ LR532 [sr]	2.39	2.47	8.30	2.79	1.45	3.12	2.05	3.33	4.20	3.42	5.18
BAE355/532	1.20	1.32	1.32	1.25	1.29	1.11	0.79	0.99	1.16	1.06	0.90
σ BAE355/532	0.06	0.04	0.06	0.08	0.03	0.03	0.04	0.02	0.03	0.03	0.06
BAE532/1064	2.04	1.92	2.04	1.90	1.81	1.64	1.48	1.76	1.37	1.61	1.64
σ BAE532/1064	0.04	0.03	0.04	0.05	0.02	0.02	0.02	0.01	0.02	0.02	0.03
EAE	**1.45**	**1.22**	**0.71**	**1.61**	1.39	**1.65**	1.34	**0.72**	**2.08**	**0.93**	0.98
σ EAE	0.15	0.14	0.31	0.20	0.08	0.22	0.16	0.16	0.27	0.18	0.33
CRLR	**0.90**	**1.04**	**1.28**	**0.86**	0.96	**0.80**	0.80	**1.11**	**0.69**	**1.06**	0.97
σ CRLR	0.06	0.06	0.16	0.07	0.03	0.07	0.05	0.07	0.08	0.08	0.13
CRBAE	1.70	1.46	1.54	1.52	1.41	1.48	1.88	1.78	1.18	1.51	1.81
σ CRBAE	0.09	0.05	0.07	0.11	0.04	0.04	0.09	0.04	0.04	0.05	0.14

Table 6. *Cont.*

Date	20140807	20140807	20140807	20140807	20140807	20160725	20160725	20160725	20170710	20170807	20170807
AE 440/675	1.79	1.79	1.79	1.79	1.79	1.46	1.46	1.46	1.36	1.66	1.66
FMF	0.91	0.91	0.91	0.91	0.91	0.94	0.94	0.94	0.63	0.82	0.82
BC max BB [%]	20.35	20.35	20.35	19.6	19.6	28.55	29.37	29.37			
BC conc. max BB [$\mu g/m^3$]	3.52	3.52	3.52	3.05	3.05	1.4	2.24	2.24			
smoke type	fresh	aged	aged	fresh	fresh/aged	fresh	fresh	aged	fresh	aged	aged

mass conc. = mass concentration, σ = uncertainty, agric. = agriculture, Rsa = rate of smoke emission, BC = black carbon, BB = biomass burning.

The mass concentration in the layer was estimated by converting the particle extinction coefficient using the conversion factor of 1.77×10^{-7} m (uncertainty 1.6×10^{-8}) and smoke density of 1.5 g/cm^3 (uncertainty 0.3 g/cm^3) [79]. The values are compared with FLEXPART calculations (see mass conc. agric.). The values are similar (within error bars and a relative difference of ~20%) except for the 25 July 2016 19 UTC lower layer (difference of 48%) and the last two layers for 7 August 2017 (~44% and ~27% difference, respectively).

In four cases, the number of fires (and detections) is quite large (from 19 to 35 fires), while the median travel time corresponding to the fires which defined the EPVT is the largest (~2.3–2.4 days). These fires are located in Eastern Ukraine and occurred on 7 August 2014 (first two cases) and 7 August 2017 (last two cases). However, the fires' location in 2014 and 2017 is slightly different. For the rest of the cases, the number of fires is below ten, while the travel time is smaller (except one case). Rsa has large values (>20 kg s^{-1}) for the cases where a large number of fires contribute to the smoke layer. We observe also that Rsa = 23.34 kg s^{-1} for the case where nine fires were observed (25 July 2016~19:00 UTC, lower layer).

The Ångström exponent from photometer AE440/675 is the largest (1.79 at 15:09, 1.80 ± 0.03 (1σ) daily averages) for the event which occurred on 7 August 2014 (18 and 19 UTC), which implies a small effective radius for smoke particles. The FMF value is 0.91 at 15:09 UTC (0.92 ± 0.01 (1σ) daily average), which indicates a major contribution from fine particles. For the next event (25 July 2016 18 and 19 UTC), AE440/675 is smaller (1.46) while FMF is larger, as was shown in Section 3.1. It implies more contribution from fine particles, but the size is slightly larger. The smallest AE and FMF are observed for the event from 10 July 2017~20:00 UTC (larger particles and less contribution). For the last event (7 August 2017~18:00 UTC), AE is 1.66 and FMF is 0.82. Overall, the contribution of FMF is predominant but the size of the particles is slightly different (as indicated by AE).

For the event where aethalometer data were available, the total BC maximum concentration, computed on the time slot when BC_{bb} fraction increased, ranges between 1.4 and 3.52 μg m^{-3}. In terms of relative concentrations, the BC fraction that resulted from biomass burning was between 19.6% and 29.37%, with the higher contribution being recorded for 25 July 2016 events. Due to the increased percentage of BC_{bb} recorded for most of the events, similar to previous findings for remote areas affected by vegetation fires in summer [77], we can speculate that BC_{bb} ground-level concentrations can be influenced by long range transport. A larger percentage is linked with large FMF, which needs to be further investigated for an increased number of cases.

4. Conclusions

Eleven smoke layers (from six hourly Raman lidar measurements) in 2014, 2016, and 2017 were analyzed. The intensive parameters in the smoke layers were investigated in connection with the effective predominant vegetation type of the burned area. The aerosol pollution layers were labeled as smoke layers if there were fires along the mean back-trajectory and the injection height from those fires was above the air mass trajectory. The mean back-trajectory was determined from an ensemble of back-trajectories using Cluster Analysis from HYSPLIT. The ensemble was composed of at least 30 altitude levels within the pollution layer. In addition to the HYSPLIT back-trajectory, the ERA5 reanalysis was used to determine the mean air flow. FLEXPART analysis was used to estimate the source–receptor sensitivity. In addition, FLEXPART showed the agricultural waste burning as the main source for all 11 smoke layers. All three complementary analyses were in good agreement.

We tackled the complex state of the mixed smoke, which is usually recorded by a remote lidar. EPVT was selected as the PVT which contributes the most to the smoke emission. Recall that in most of the cases, there are several fires contributing to the smoke measurements. For the current cases, the EPVT was either type II (grasses/cereal) or type IV (broadleaf crops), which can be seen as part of the broader category of agricultural crops. The IPs are similar and thus we can assign the findings for both types in the larger

group of agricultural crops. The travel time (corresponding to the fires which determined the EPVT) was between 0.31 days and 2.4 days. The EAE–CR_{LR} correlation was in good agreement (within error bars) with the labeling of fresh versus aged smoke based on both EAE and CR_{LR} values. While the median of the travel time for fresh smoke was 1.65 days and for aged smoke was 2.4 days, we observed a case of 2.4 days for fresh smoke and 1.1 days for aged smoke. However, the case of 2.4 days can be labeled as a mixture of fresh and aged smoke (EAE = 1.39 and CR_{LR} = 0.96). In the case of 1.1 days, we speculate that the aging may be due to high RH along the trajectory (Figure S7). Thus, the travel time should be used along with EAE and CR_{LR} values to categorize the smoke as fresh or aged. The aging depends on the photochemistry processes along the transportation. Based on laboratory experiments on smoldering combustion, Chen et al. [80] showed that fresh peatland particles are oxidized faster (aged) at elevated RH, while the chemical aging occurs faster for smaller particles.

Most of the fires analyzed in our study were located in Ukraine, which is one of the main sources for transported BB smoke at our location. Based on the air mass climatology over 2008–2018 (not shown here), the predominant circulation types for our site are from the northwest (43.7%) and western (25.7%). However, most of the biomass burning transported to our site occurs in the Balkans and Ukraine/West Russia. We have a more frequent circulation from the north (17.4%), northeast (4.7%), and east (1.1%) as compared with southwest (5.4%) and south (1.3%). Thus, there are more chances to measure fires from Ukraine and West Russia than from the Balkans.

LR355 and EAE tend to decrease with travel time, while CR_{LR}, BAE, and CR_{BAE} tend to increase with travel time (where the travel time is less than three days).

The photometer values for AE and FMF show the presence of fine particles, which is a characteristic of smoke. AE 440/675 ranges between 1.36 and 1.79, while FMF is always higher than 0.8, except in the event from 10 July 2017~20:00 UTC. However, the fire from this event is in close proximity to INOE (smoke travel time 0.31 days) and it is associated with the lowest rate of smoke emission (3.20). The close distance of the fire contributed to the smoke detection from the lidar measurements, but at the same time the low emission rate maintained relatively low the levels of FMF. The in situ BC measurements available for four out of six lidar profiles show a possible PBL contamination from the smoke layers in the following 24 h from the lidar measurements.

Future investigation aims to characterize other types of vegetation besides types II and IV and thus to extract potential different signatures in terms of IPs. The ceilometer continuous monitoring, available since 2018, will allow to assess the circumstances when the pollution layers penetrate into the PBL. The methodology developed and shown here for two types can be applied to any type of vegetation.

Supplementary Materials: The following supporting information can be downloaded at: https://www.mdpi.com/article/10.3390/rs14194734/s1, which shows the HYSPLIT back-trajectories, ERA5 reanalysis, and FELXAPRT source–receptor sensitivity for all the cases analyzed.

Author Contributions: Conceptualization, M.A. and K.F.; methodology, M.A.; software, M.A., K.F., L.B., S.S., C.T., V.N. and S.A.; validation, M.A. and K.F.; formal analysis, M.A. and K.F.; investigation, M.A. and K.F.; resources, M.A., K.F., S.S., S.A., C.T., L.M., V.N., L.B. and D.E.; data curation, M.A. and K.F.; writing—original draft preparation, M.A. and K.F.; writing—review and editing, B.A., S.S., L.M., D.E. and V.A.; visualization, M.A., S.A. and C.T.; supervision, M.A., K.F. and B.A.; project administration, M.A.; funding acquisition, M.A. and C.T. All authors have read and agreed to the published version of the manuscript.

Funding: This research was mainly funded by The Executive Agency for Higher Education, Research, Development and Innovation Funding (UEFISCDI), PN-III-P2-2.1-PED-2019-1816, contract number 458PED/2020, and partly by 295PED/2020. Part of the work performed for this study was funded by the Romanian National Core Program Contract No.18N/2019 and by the Romanian Ministry of Research, Innovation and Digitalization, through Program 1—Development of the national research-development system, Subprogram 1.2—Institutional performance—Projects to finance the excellent RDI, Contract no. 18PFE/30.12.2021, by the European Regional Development Fund through the

Competitiveness Operational Programme 2014–2020, Action 1.1.3, Creating synergies with H2020 Programme, the project Strengthen the participation of the ACTRIS-RO consortium in the pan-European research infrastructure ACTRIS, ACTRIS-ROC, MYSMIS code 107596 (contract No.337/2021), and by European Regional Development Fund through the Competitiveness Operational Programme 2014–2020, POC-A.1-A.1.1.1- F-2015, project Research Centre for Environment and Earth Observation CEO-Terra, SMIS code 108109, contract No. 152/2016.

Data Availability Statement: The MODIS FIRMS and land cover data are publicly available. For the other data or information, please contact the authors.

Acknowledgments: GFAS data were generated using Copernicus Atmosphere Monitoring Service Information, operated by the ECMWF. We also thank NOAA Air Resources Laboratory (ARL) for the provision of the HYSPLIT transport and dispersion model and/or READY website (http://www.ready.noaa.gov, last access: 6 April 2022) and ECCAD—Emissions of Atmospheric Compounds and Compilation of Ancillary Data (https://eccad3.sedoo.fr/, last access 21 July 2022). Authors acknowledge AERONET-Europe for providing calibration service. AERONET-Europe is part of the ACTRIS-IMP project that received funding from the European Union (H2020-INFRADEV-2018–2020) under Grant Agreement No. 871115. Authors also acknowledge the Barcelona Supercomputing Center for the data and/or images from the (BSC-DREAM8b) model, operated by the Barcelona Supercomputing Center (http://www.bsc.es/ess/bsc-dust-daily-forecast/ (accessed on 12 July 2022)). We would also like to thank the three anonymous reviewers for their constructive comments that helped us to improve the original manuscript.

Conflicts of Interest: The authors declare no conflict of interest.

References

1. Fiebig, M.; Petzold, A.; Wandinger, U.; Wendisch, M.; Kiemle, C.; Stifter, A.; Ebert, M.; Rother, T.; Leiterer, U. Optical closure for an aerosol column: Method, accuracy, and inferable properties applied to a biomass-burning aerosol and its radiative forcing. *J. Geophys. Res.* **2002**, *107*, LAC 12-1–LAC 12-15. [CrossRef]
2. Adam, M.; Pahlow, M.; Kovalev, V.A.; Ondov, J.M.; Parlange, M.B.; Nair, N. Aerosol optical characterization by nephelometer and lidar: The Baltimore Supersite experiment during the Canadian forest fire smoke intrusion. *J. Geophys. Res.* **2004**, *109*, D16S02. [CrossRef]
3. Sapkota, A.; Symons, J.M.; Kleissl, J.; Wang, L.; Parlange, M.B.; Ondov, J.; Breysse, P.N.; Diette, G.B.; Eggleston, P.A.; Buckley, T. Impact of the 2002 Canadian Forest Fires on Particulate Matter Air Quality in Baltimore City. *Environ. Sci. Technol.* **2002**, *39*, 24–32. [CrossRef]
4. Alonso-Blanco, E.; Castro, A.; Calvo, A.I.; Pont, V.; Mallet, M.; Fraile, R. Wildfire smoke plumes transport under a subsidence inversion: Climate and health implications in a distant urban area. *Sci. Total Environ.* **2018**, *619–620*, 988–1002. [CrossRef] [PubMed]
5. Nicolae, V.; Talianu, C.; Andrei, S.; Antonescu, B.; Ene, D.; Nicolae, D.; Dandocsi, A.; Toader, V.-E.; Ștefan, S.; Savu, T.; et al. Multiyear Typology of Long-Range Transported Aerosols over Europe. *Atmosphere* **2019**, *10*, 482. [CrossRef]
6. Shi, S.; Cheng, T.; Gu, X.; Guo, H.; Wu, Y.; Wang, Y. Biomass burning aerosol characteristics for different vegetation types in different aging periods. *Environ. Int.* **2019**, *126*, 504–511. [CrossRef] [PubMed]
7. Vadrevu, K.P.; Lasko, K.; Giglio, L.; Justice, C. Vegetation fires, absorbing aerosols and smoke plume characteristics in diverse biomass burning regions of Asia. *Environ. Res. Lett.* **2015**, *10*, 105003. [CrossRef]
8. Junghenn Noyes, K.T.; Kahn, R.A.; Limbacher, J.A.; Li, Z.; Fenn, M.A.; Giles, D.M.; Hair, J.W.; Katich, J.M.; Moore, R.H.; Robinson, C.E.; et al. Wildfire Smoke Particle Properties and Evolution, from Space-Based Multi-Angle Imaging II: The Williams Flats Fire during the FIREX-AQ Campaign. *Remote Sens.* **2020**, *12*, 3823. [CrossRef]
9. Smith, D.M.; Fiddler, M.N.; Pokhrel, R.P.; Bililign, S. Laboratory studies of fresh and aged biomass burning aerosol emitted from east African biomass fuels—Part 1: Optical properties. *Atmos. Chem. Phys.* **2020**, *20*, 10149–10168. [CrossRef]
10. Capes, G.; Johnson, B.; McFiggans, G.; Williams, P.I.; Haywood, J.; Coe, H. Aging of biomass burning aerosols over West Africa: Aircraft measurements of chemical composition, microphysical properties, and emission ratios. *J. Geophys. Res. Atmos.* **2008**, *113*, D00C15. [CrossRef]
11. Radenz, M.; Seifert, P.; Baars, H.; Floutsi, A.A.; Yin, Z.; Bühl, J. Automated time–height-resolved air mass source attribution for profiling remote sensing applications. *Atmos. Chem. Phys.* **2021**, *21*, 3015–3033. [CrossRef]
12. Floutsi, A.A.; Baars, H.; Radenz, M.; Haarig, M.; Yin, Z.; Seifert, P.; Jimenez, C.; Ansmann, A.; Engelmann, R.; Barja, B.; et al. Advection of Biomass Burning Aerosols towards the Southern Hemispheric Mid-Latitude Station of Punta Arenas as Observed with Multiwavelength Polarization Raman Lidar. *Remote Sens.* **2021**, *13*, 138. [CrossRef]
13. Heese, B.; Floutsi, A.A.; Baars, H.; Althausen, D.; Hofer, J.; Herzog, A.; Mewes, S.; Radenz, M.; Schechner, Y.Y. The vertical aerosol type distribution above Israel—2 years of lidar observations at the coastal city of Haifa. *Atmos. Chem. Phys.* **2022**, *22*, 1633–1648. [CrossRef]

14. Val Martin, M.; Kahn, R.A.; Tosca, M.G. A Global Analysis of Wildfire Smoke Injection Heights Derived from Space-Based Multi-Angle Imaging. *Remote Sens.* **2018**, *10*, 1609. [CrossRef]
15. Amiridis, V.; Balis, D.S.; Giannakaki, E.; Stohl, A.; Kazadzis, S.; Koukouli, M.E.; Zanis, P. Optical characteristics of biomass burning aerosols over Southeastern Europe determined from UV-Raman lidar measurements. *Atmos. Chem. Phys.* **2009**, *9*, 2431–2440. [CrossRef]
16. Stohl, A.; Berg, T.; Burkhart, J.F.; Fjæraa, A.M.; Forster, C.; Herber, A.; Hov, Ø.; Lunder, C.; McMillan, W.W.; Oltmans, S.; et al. Arctic smoke–record high air pollution levels in the European Arctic due to agricultural fires in Eastern Europe in spring 2006. *Atmos. Chem. Phys.* **2007**, *7*, 511–534. [CrossRef]
17. Seiler, W.; Crutzen, P.J. Estimates of gross and net fluxes of carbon between the biosphere and the atmosphere from biomass burning. *Clim. Chang.* **1980**, *2*, 207–247. [CrossRef]
18. Labonne, M.; Bréon, F.-M.; Chevallier, F. Injection height of biomass burning aerosols as seen from a spaceborne lidar. *Geophys. Res. Lett.* **2007**, *34*. [CrossRef]
19. Val Martin, M.; Logan, J.A.; Kahn, R.A.; Leung, F.Y.; Nelson, D.L.; Diner, D.J. Smoke injection heights from fires in North America: Analysis of 5 years of satellite observations. *Atmos. Chem. Phys.* **2010**, *10*, 1491–1510. [CrossRef]
20. Amiridis, V.; Giannakaki, E.; Balis, D.S.; Gerasopoulos, E.; Pytharoulis, I.; Zanis, P.; Kazadzis, S.; Melas, D.; Zerefos, C. Smoke injection heights from agricultural burning in Eastern Europe as seen by CALIPSO. *Atmos. Chem. Phys.* **2010**, *10*, 11567–11576. [CrossRef]
21. Pappalardo, G.; Amodeo, A.; Apituley, A.; Comeron, A.; Freudenthaler, V.; Linné, H.; Ansmann, A.; Bösenberg, J.; D'Amico, G.; Mattis, I.; et al. EARLINET: Towards an advanced sustainable European aerosol lidar network. *Atmos. Meas. Tech.* **2014**, *7*, 2389–2409. [CrossRef]
22. Sicard, M.; Granados-Muñoz, M.J.; Alados-Arboledas, L.; Barragán, R.; Bedoya-Velásquez, A.E.; Benavent-Oltra, J.A.; Bortoli, D.; Comerón, A.; Córdoba-Jabonero, C.; Costa, M.J.; et al. Ground/space, passive/active remote sensing observations coupled with particle dispersion modelling to understand the inter-continental transport of wildfire smoke plumes. *Remote Sens. Environ.* **2019**, *232*, 111294. [CrossRef]
23. Baars, H.; Ansmann, A.; Ohneiser, K.; Haarig, M.; Engelmann, R.; Althausen, D.; Hanssen, I.; Gausa, M.; Pietruczuk, A.; Szkop, A.; et al. The unprecedented 2017–2018 stratospheric smoke event: Decay phase and aerosol properties observed with the EARLINET. *Atmos. Chem. Phys.* **2019**, *19*, 15183–15198. [CrossRef]
24. Mamouri, R.E.; Papayannis, A.; Amiridis, V.; Müller, D.; Kokkalis, P.; Rapsomanikis, S.; Karageorgos, E.T.; Tsaknakis, G.; Nenes, A.; Kazadzis, S.; et al. Multi-wavelength Raman lidar, sun photometric and aircraft measurements in combination with inversion models for the estimation of the aerosol optical and physico-chemical properties over Athens, Greece. *Atmos. Meas. Tech.* **2012**, *5*, 1793–1808. [CrossRef]
25. Nicolae, D.; Nemuc, A.; Müller, D.; Talianu, C.; Vasilescu, J.; Belegante, L.; Kolgotin, A. Characterization of fresh and aged biomass burning events using multiwavelength Raman lidar and mass spectrometry. *J. Geophys. Res.-Atmos.* **2013**, *118*, 2956–2965. [CrossRef]
26. Nepomuceno Pereira, S.; Preißler, J.; Guerrero-Rascado, J.L.; Silva, A.M.; Wagner, F. Forest Fire Smoke Layers Observed in the Free Troposphere over Portugal with a Multiwavelength Raman Lidar: Optical and Microphysical Properties. *Sci. World J.* **2014**, *2014*, 421838. [CrossRef]
27. Samaras, S.; Nicolae, D.; Böckmann, C.; Vasilescu, J.; Binietoglou, I.; Labzovskii, L.; Toanca, F.; Papayannis, A. Using Raman-lidar-based regularized microphysical retrievals and Aerosol Mass Spectrometer measurements for the characterization of biomass burning aerosols. *J. Comput. Phys.* **2015**, *299*, 156–174. [CrossRef]
28. Mylonaki, M.; Papayannis, A.; Anagnou, D.; Veselovskii, I.; Papanikolaou, C.-A.; Kokkalis, P.; Soupiona, O.; Foskinis, R.; Gidarakou, M.; Kralli, E. Optical and Microphysical Properties of Aged Biomass Burning Aerosols and Mixtures, Based on 9-Year Multiwavelength Raman Lidar Observations in Athens, Greece. *Remote Sens.* **2021**, *13*, 3877. [CrossRef]
29. Stachlewska, I.S.; Samson, M.; Zawadzka, O.; Harenda, K.M.; Janicka, L.; Poczta, P.; Szczepanik, D.; Heese, B.; Wang, D.; Borek, K.; et al. Modification of Local Urban Aerosol Properties by Long-Range Transport of Biomass Burning Aerosol. *Remote Sens.* **2018**, *10*, 412. [CrossRef]
30. Müller, D.; Mattis, I.; Wandinger, U.; Ansmann, A.; Althausen, D.; Stohl, A. Raman lidar observations of aged Siberian and Canadian forest fire smoke in the free troposphere over Germany in 2003: Microphysical particle characterization. *J. Geophys. Res.* **2005**, *110*, D17201. [CrossRef]
31. Vaughan, G.; Draude, A.P.; Ricketts, H.M.A.; Schultz, D.M.; Adam, M.; Sugier, J.; Wareing, D.P. Transport of Canadian forest fire smoke over the UK as observed by lidar. *Atmos. Chem. Phys.* **2018**, *18*, 11375–11388. [CrossRef]
32. Ortiz-Amezcua, P.; Guerrero-Rascado, J.L.; Granados-Muñoz, M.J.; Benavent-Oltra, J.A.; Böckmann, C.; Samaras, S.; Stachlewska, I.S.; Janicka, Ł.; Baars, H.; Bohlmann, S.; et al. Microphysical characterization of long-range transported biomass burning particles from North America at three EARLINET stations. *Atmos. Chem. Phys.* **2017**, *17*, 5931–5946. [CrossRef]
33. Haarig, M.; Ansmann, A.; Baars, H.; Jimenez, C.; Veselovskii, I.; Engelmann, R.; Althausen, D. Depolarization and lidar ratios at 355, 532, and 1064 nm and microphysical properties of aged tropospheric and stratospheric Canadian wildfire smoke. *Atmos. Chem. Phys.* **2018**, *18*, 11847–11861. [CrossRef]

34. Markowicz, K.M.; Chilinski, M.T.; Lisok, J.; Zawadzka, O.; Stachlewska, I.S.; Janicka, L.; Rozwadowska, A.; Makuch, P.; Pakszys, P.; Zielinski, T.; et al. Study of aerosol optical properties during long-range transport of biomass burning from Canada to Central Europe in July 2013. *J. Aerosol Sci.* **2016**, *101*, 156–173. [CrossRef]
35. Markowicz, K.M.; Pakszys, P.; Ritter, C.; Zielinski, T.; Udisti, R.; Cappelletti, D.; Mazzola, M.; Shiobara, M.; Xian, P.; Zawadzka, O.; et al. Impact of North American intense fires on aerosol optical properties measured over the European Arctic in July 2015. *J. Geophys. Res. Atmos.* **2016**, *121*, 14487–14512. [CrossRef]
36. Hu, Q.; Goloub, P.; Veselovskii, I.; Bravo-Aranda, J.A.; Popovici, I.E.; Podvin, T.; Haeffelin, M.; Lopatin, A.; Dubovik, O.; Pietras, C.; et al. Long-range-transported Canadian smoke plumes in the lower stratosphere over northern France. *Atmos. Chem. Phys.* **2019**, *19*, 1173–1193. [CrossRef]
37. Adam, M.; Nicolae, D.; Stachlewska, I.S.; Papayannis, A.; Balis, D. Biomass burning events measured by lidars in EARLINET—Part 1: Data analysis methodology. *Atmos. Chem. Phys.* **2020**, *20*, 13905–13927. [CrossRef]
38. Nemuc, A.; Vasilescu, J.; Talianu, C.; Belegante, L.; Nicolae, D. Assessment of aerosol's mass concentrations from measured linear particle depolarization ratio (vertically resolved) and simulations. *Atmos. Meas. Tech.* **2013**, *6*, 3243–3255. [CrossRef]
39. D'Amico, G.; Amodeo, A.; Baars, H.; Binietoglou, I.; Freudenthaler, V.; Mattis, I.; Wandinger, U.; Pappalardo, G. EARLINET Single Calculus Chain—Overview on methodology and strategy. *Atmos. Meas. Tech.* **2015**, *8*, 4891–4916. [CrossRef]
40. D'Amico, G.; Amodeo, A.; Mattis, I.; Freudenthaler, V.; Pappalardo, G. EARLINET Single Calculus Chain—technical—Part 1: Pre-processing of raw lidar data. *Atmos. Meas. Tech.* **2016**, *9*, 491–507. [CrossRef]
41. Mattis, I.; D'Amico, G.; Baars, H.; Amodeo, A.; Madonna, F.; Iarlori, M. EARLINET Single Calculus Chain—technical—Part 2: Calculation of optical products. *Atmos. Meas. Tech.* **2016**, *9*, 3009–3029. [CrossRef]
42. Adam, M.; Nicolae, V.; Boldeanu, M. Algorithm to determine the aerosol pollution layers from ceilometer profiles. In Proceedings of the European Lidar Conference ELC2021, Granada, Spain, 16–18 November 2021; p. S02P12.
43. Adam, M.; Fragkos, K.; Binietoglou, I.; Wang, D.; Stachlewska, I.S.; Belegante, L.; Nicolae, V. Towards Early Detection of Tropospheric Aerosol Layers Using Monitoring with Ceilometer, Photometer, and Air Mass Trajectories. *Remote Sens.* **2022**, *14*, 1217. [CrossRef]
44. MathWorks. Available online: https://www.mathworks.com/help/matlab/ref/islocalmin.html?s_tid=srchtitle_islocalmin_1 (accessed on 12 July 2022).
45. Rolph, G.; Stein, A.; Sunder, B. Real-time Environmental Applications and Display sYstem: READY. *Environ. Modell. Softw.* **2017**, *95*, 210–228. [CrossRef]
46. Stein, A.F.; Draxler, R.R.; Rolph, G.D.; Stunder, B.J.B.; Cohen, M.D.; Ngan, F. NOAA's HYSPLIT Atmospheric Transport and Dispersion Modeling System. *Bull. Amer. Meteor. Soc.* **2015**, *96*, 2059–2077. [CrossRef]
47. Janicka, L.; Stachlewska, I.S.; Veselovskii, I.; Baars, H. Temporal variations in optical and microphysical properties of mineral dust and biomass burning aerosol derived from daytime Raman lidar observations over Warsaw, Poland. *Atmos. Environ.* **2017**, *169*, 162–174. [CrossRef]
48. Ohneiser, K.; Ansmann, A.; Baars, H.; Seifert, P.; Barja, B.; Jimenez, C.; Radenz, M.; Teisseire, A.; Floutsi, A.; Haarig, M.; et al. Smoke of extreme Australian bushfires observed in the stratosphere over Punta Arenas, Chile, in January 2020: Optical thickness, lidar ratios, and depolarization ratios at 355 and 532 nm. *Atmos. Chem. Phys.* **2020**, *20*, 8003–8015. [CrossRef]
49. Sitnov, S.A.; Mokhov, I.I.; Gorchakov, G.I.; Dzhola, A.V. Smoke Haze over the European part of Russia in the Summer of 2016: A Link to Wild fires in Siberia and Atmospheric Circulation Anomalies. *Russ. Meteorol. Hydrol.* **2017**, *42*, 518–528. [CrossRef]
50. Engelmann, R.; Ansmann, A.; Ohneiser, K.; Griesche, H.; Radenz, M.; Hofer, J.; Althausen, D.; Dahlke, S.; Maturilli, M.; Veselovskii, I.; et al. Wildfire smoke, Arctic haze, and aerosol effects on mixed-phase and cirrus clouds over the North Pole region during MOSAiC: An introduction. *Atmos. Chem. Phys.* **2021**, *21*, 13397–13423. [CrossRef]
51. Ohneiser, K.; Ansmann, A.; Chudnovsky, A.; Engelmann, R.; Ritter, C.; Veselovskii, I.; Baars, H.; Gebauer, H.; Griesche, H.; Radenz, M.; et al. The unexpected smoke layer in the High Arctic winter stratosphere during MOSAiC 2019–2020. *Atmos. Chem. Phys.* **2021**, *21*, 15783–15808. [CrossRef]
52. Quaglia, F.C.; Meloni, D.; Muscari, G.; Di Iorio, T.; Ciardini, V.; Pace, G.; Becagli, S.; Di Bernardino, A.; Cacciani, M.; Hannigan, J.W.; et al. On the Radiative Impact of Biomass-Burning Aerosols in the Arctic: The August 2017 Case Study. *Remote Sens.* **2022**, *14*, 313. [CrossRef]
53. ARL. *Global Data Assimilation System (GDAS1) Archive Information*; ARL: Washington, DC, USA, 2004.
54. Radenz, M.; Zhenping, Y. ARLreader Python Library. Available online: https://github.com/martin-rdz/ARLreader (accessed on 12 July 2022).
55. Hersbach, H.; Bell, B.; Berrisford, P.; Hirahara, S.; Horányi, A.; Muñoz-Sabater, J.; Nicolas, J.; Peubey, C.; Radu, R.; Schepers, D.; et al. The ERA5 global reanalysis. *Q. J. R. Meteorol. Soc.* **2020**, *146*, 1999–2049. [CrossRef]
56. Chen, Y.; Sharma, S.; Zhou, X.; Yang, K.; Li, X.; Niu, X.; Hu, X.; Khadka, N. Spatial performance of multiple reanalysis precipitation datasets on the southern slope of central Himalaya. *Atmos. Res.* **2021**, *250*, 106365. [CrossRef]
57. Dong, Z.; Jin, S. Evaluation of Spaceborne GNSS-R Retrieved Ocean Surface Wind Speed with Multiple Datasets. *Remote Sens.* **2019**, *11*, 2747. [CrossRef]
58. Davies, D.K.; Ilavajhala, S.; Wong, M.M.; Justice, C.O. Fire Information for Resource Management System: Archiving and Distributing MODIS Active Fire Data. *IEEE T. Geosci. Remote* **2009**, *47*, 72–79. [CrossRef]

59. Kaiser, J.W.; Heil, A.; Andreae, M.O.; Benedetti, A.; Chubarova, N.; Jones, L.; Morcrette, J.J.; Razinger, M.; Schultz, M.G.; Suttie, M.; et al. Biomass burning emissions estimated with a global fire assimilation system based on observed fire radiative power. *Biogeosciences* **2012**, *9*, 527–554. [CrossRef]
60. Kaiser, J.W.; Suttie, M.; Flemming, J.; Morcrette, J.J.; Boucher, O.; Schultz, M.G. Global Real-time Fire Emission Estimates Based on Space-borne Fire Radiative Power Observations. In Proceedings of the Current Problems in Atmospheric Radiation (IRS 2008) and International Radiation Symposium (IRC/IAMAS), Foz do Iguaçu Brazil, 3–8 August 2008; pp. 645–648.
61. Freeborn, P.; Wooster, M.; Roy, D.; Cochrane, M. Quantification of MODIS fire radiative power (FRP) measurement uncertainty for use in satellite-based active fire characterization and biomass burning estimation. *Geophys. Res. Lett.* **2014**, *41*, 1988–1994. [CrossRef]
62. Rémy, S.; Veira, A.; Paugam, R.; Sofiev, M.; Kaiser, J.W.; Marenco, F.; Burton, S.P.; Benedetti, A.; Engelen, R.J.; Ferrare, R.; et al. Two global data sets of daily fire emission injection heights since 2003. *Atmos. Chem. Phys.* **2017**, *17*, 2921–2942. [CrossRef]
63. Di Giuseppe, F.; Rémy, S.; Pappenberger, F.; Wetterhall, F. Using the Fire Weather Index (FWI) to improve the estimation of fire emissions from fire radiative power (FRP) observations. *Atmos. Chem. Phys.* **2018**, *18*, 5359–5370. [CrossRef]
64. Sulla-Menashe, D.; Friedl, M.A. User Guide to Collection 6 MODIS Land Cover (MCD12Q1 and MCD12C1) Product. Available online: https://lpdaac.usgs.gov/documents/101/MCD12_User_Guide_V6.pdf (accessed on 6 June 2022).
65. NASA. Fire Energetics and Emissions Research. Available online: https://feer.gsfc.nasa.gov/data/emissions/ (accessed on 6 June 2022).
66. Stohl, A.; Forster, C.; Frank, A.; Seibert, P.; Wotawa, G. Technical note: The Lagrangian particle dispersion model FLEXPART version 6.2. *Atmos. Chem. Phys.* **2005**, *5*, 2461–2474. [CrossRef]
67. Seibert, P.; Frank, A. Source-receptor matrix calculation with a Lagrangian particle dispersion model in backward mode. *Atmos. Chem. Phys.* **2004**, *4*, 51–63. [CrossRef]
68. Pisso, I.; Sollum, E.; Grythe, H.; Kristiansen, N.I.; Cassiani, M.; Eckhardt, S.; Arnold, D.; Morton, D.; Thompson, R.L.; Groot Zwaaftink, C.D.; et al. The Lagrangian particle dispersion model FLEXPART version 10.4. *Geosci. Model Dev.* **2019**, *12*, 4955–4997. [CrossRef]
69. ECCAD. Emissions of atmospheric Compounds and Compilation of Ancillary Data. Available online: https://eccad.aeris-data.fr/ (accessed on 12 July 2022).
70. Holben, B.N.; Eck, T.F.; Slutsker, I.; Tanre, D.; Buis, J.P.; Setzer, A.; Vermote, E.; Reagan, J.A.; Kaufman, Y.J.; Nakajima, T.; et al. AERONET—A federated instrument network and data archive for aerosol characterization. *Remote Sens. Env.* **1998**, *66*, 1–16. [CrossRef]
71. Carstea, E.; Fragkos, E.; Siomos, N.; Antonescu, B.; Belegante, L. Columnar aerosol measurements in a continental southeastern Europe site: Climatology and trends. *Theor. Appl. Climatol.* **2019**, *137*, 3149–3159. [CrossRef]
72. Barreto, Á.; Cuevas, E.; Granados-Muñoz, M.J.; Alados-Arboledas, L.; Romero, P.M.; Gröbner, J.; Kouremeti, N.; Almansa, A.F.; Stone, T.; Toledano, C.; et al. The new sun-sky-lunar Cimel CE318-T multiband photometer—A comprehensive performance evaluation. *Atmos. Meas. Tech.* **2016**, *9*, 631–654. [CrossRef]
73. Holben, B.N.; Tanre, D.; Smirnov, A.; Eck, T.F.; Slutsker, I.; Abuhassan, N.; Newcomb, W.W.; Schafer, J.S.; Chatenet, B.; Lavenu, F.; et al. An emerging ground-based aerosol climatology: Aerosol optical depth from AERONET. *J. Geophys. Res.* **2011**, *106*, 12067–12097. [CrossRef]
74. O'Neill, N.T.; Eck, T.F.; Smirnov, A.; Holben, B.N.; Thulasiraman, S. Spectral discrimination of coarse and fine mode optical depth. *J. Geophys. Res.* **2003**, *108*, 4559. [CrossRef]
75. Giles, D.M.; Sinyuk, A.; Sorokin, M.G.; Schafer, J.S.; Smirnov, A.; Slutsker, I.; Eck, T.F.; Holben, B.N.; Lewis, J.R.; Campbell, J.R.; et al. Advancements in the Aerosol Robotic Network (AERONET) Version 3 database—Automated near-real-time quality control algorithm with improved cloud screening for Sun photometer aerosol optical depth (AOD) measurements. *Atmos. Meas. Tech.* **2019**, *12*, 169–209. [CrossRef]
76. Sandradewi, J.; Prevot, A.S.H.; Weingartner, E.; Schmidhauser, R.; Gysel, M.; Baltensperger, U. A study of wood burning and traffic aerosols in an Alpine valley using a multi-wavelength Aethalometer. *Atmos. Environ.* **2008**, *42*, 101–112. [CrossRef]
77. Becerril-Valle, M.; Coz, E.; Prevot, A.S.H.; Mocnik, G.; Pandis, S.N.; de la Campa, A.M.S.; Alastuey, A.; Diaz, E.; Perez, R.M.; Artinano, B. Characterization of atmospheric black carbon and co-pollutants in urban and rural areas of Spain. *Atmos. Environ.* **2017**, *169*, 36–53. [CrossRef]
78. Müller, D.; Mattis, I.; Ansmann, A.; Wandinger, U.; Ritter, C.; Kaiser, D. Multiwavelength Raman lidar observations of particle growth during long-range transport of forest-fire smoke in the free troposphere. *Geophys. Res. Lett.* **2007**, *34*, L05803. [CrossRef]
79. Ansmann, A.; Tesche, M.; Seifert, P.; Groß, S.; Freudenthaler, V.; Apituley, A.; Wilson, K.M.; Serikov, I.; Linné, H.; Heinold, B.; et al. Ash and fine-mode particle mass profiles from EARLINET-AERONET observations over central Europe after the eruptions of the Eyjafjallajökull volcano in 2010. *J. Geophys. Res. Atmos.* **2011**, *116*, D00U02. [CrossRef]
80. Chen, J.; Budisulistiorini, S.H.; Itoh, M.; Kuwata, M. Roles of Relative Humidity and Particle Size on Chemical Aging of Tropical Peatland Burning Particles: Potential Influence of Phase State and Implications for Hygroscopic Property. *J. Geophys. Res. Atmos.* **2022**, *127*, e2022JD036871. [CrossRef]